Reaction Chemistry & Engineering

ROYAL SOCIETY OF CHEMISTRY

PAPER

View Article Online
View Journal | View Issue

Cite this: *React. Chem. Eng.*, 2024, **9**, 1933

Optimizing CO_2 methanation: effect of surface basicity and active phase reducibility on Ni-based catalysts

Marie-Nour Kaydouh, [a] Nissrine El Hassan, *[a] Ahmed I. Osman, *[b] Hamid Ahmed, [c] Naif Alarifi, *[d] Anis H. Fakeeha, [c] Abdulrahman Bin Jumah [c] and Ahmed S. Al-Fatesh *[c]

CO_2 methanation presents an intriguing avenue for utilizing carbon dioxide and generating methane as synthetic natural gas. This study delves into the innovative synthesis of MgO–Al_2O_3 mixed oxide support, a Co-active phase, and either Sr or Ce promoters to enhance the performance of Ni-based catalysts in CO_2 methanation. The primary objective is to identify the optimal ratio of Mg to Al for supporting 5 wt% Ni, followed by assessing the synergistic utilization of Co and Ni, along with different promoters, on the most promising support. Despite exhibiting comparable textural and basic characteristics, the increase of Mg content in Al_2O_3 introduces a delay in NiO reduction by promoting the formation of a NiO–MgO solid solution. The $Ni_5/Mg_{63}Al_{37}$ catalyst presents the highest CO_2 conversion of 92% and CH_4 yield of 82% at 400 °C. This catalytic activity surpasses that of $Co_5/Mg_{63}Al_{37}$ and $Ni_{2.5}Co_{2.5}/Mg_{63}Al_{37}$, mainly due to easier reduction of the monometallic Ni-based sample. Examining the impact of promoters on $Ni_{2.5}Co_{2.5}/Mg_{63}Al_{37}$ catalyst reveals the advantageous influence of Ce in terms of facilitative reduction and improved basicity. However, the promoting effect of Sr remains less discernible, potentially due to the already increased basicity resulting from the utilization of the MgO–Al_2O_3 support.

Received 15th February 2024,
Accepted 18th April 2024

DOI: 10.1039/d4re00084f

rsc.li/reaction-engineering

Introduction

Carbon dioxide undergoes hydrogenation in a methanation reaction to produce methane, as depicted in eqn (1). This process is pivotal in mitigating the greenhouse effect and combating global warming. Indeed, the reduction of CO_2 emissions is nowadays a common challenge worldwide.[1] Furthermore, it offers a transition from the carbon capture and storage (CCS) strategy to a more pragmatic and favorable carbon capture and utilization (CCU) approach.[2] Depending on the specific operational conditions, this reaction may be accompanied by concurrent side reactions, as illustrated in eqn (2) to (4). These side reactions can potentially yield undesired byproducts like carbon monoxide (CO) or consume methane, consequently leading to diminished product yield and selectivity.[3] Alternatively, side reactions (eqn (5) to (9)) can also occur, resulting in solid carbon deposits that may accumulate on the catalyst surface, ultimately triggering catalyst deactivation.

$$CO_{2(g)} + 4H_{2(g)} = CH_{4(g)} + 2H_2O_{(g)} \quad (1)$$

$$CO_{2(g)} + H_{2(g)} = CO_{(g)} + H_2O_{(g)} \quad (2)$$

$$CO_{2(g)} + CH_{4(g)} = 2CO_{(g)} + 2H_{2(g)} \quad (3)$$

$$CO_{(g)} + 3H_{2(g)} = CH_{4(g)} + H_2O_{(g)} \quad (4)$$

$$CO_{2(g)} + 2H_{2(g)} = C_{(s)} + 2H_2O_{(g)} \quad (5)$$

$$CO_{2(g)} + CH_{4(g)} = 2C_{(s)} + 2H_2O_{(g)} \quad (6)$$

$$2CO_{(g)} = C_{(s)} + CO_{2(g)} \quad (7)$$

$$CH_{4(g)} = C_{(s)} + 2H_{2(g)} \quad (8)$$

$$CO_{(g)} + H_{2(g)} = C_{(s)} + H_2O_{(g)} \quad (9)$$

Kinetically speaking, CO_2 methanation can proceed *via* two suggested mechanisms: either through an associative CO_2

[a] *Petroleum Engineering Program, School of Engineering, Lebanese American University, P.O. Box 36, Byblos, Lebanon. E-mail: nissrine.elhassan@lau.edu.lb*
[b] *School of Chemistry and Chemical Engineering, Queen's University Belfast, Belfast BT9 5AG, Northern Ireland, UK. E-mail: aosmanahmed01@qub.ac.uk*
[c] *Chemical Engineering Department, College of Engineering, King Saud University, P.O. Box 800, Riyadh 11421, Saudi Arabia. E-mail: aalfatesh@ksu.edu.sa*
[d] *Institute of Refining and Petrochemicals Technologies, King Abdulaziz City for Science and Technology (KACST), P.O. Box 6086, Riyadh 11442, Kingdom of Saudi Arabia. E-mail: naalarifi@kacst.gov.sa*

methanation pathway, where CO_2 is hydrogenated to formate and then to CH_4, or through a dissociative CO_2 methanation pathway, where CO_2 is dissociated to CO*, which is then hydrogenated to CH_4.[4] In both cases, the initial step consists of CO_2 adsorption on the catalytic surface. Therefore, an efficient catalyst is essential to promote CO_2 adsorption and enhance the methanation reaction under low temperature and pressure conditions. This catalyst should also effectively suppress side reactions, prevent active metal sintering, and minimize carbon deposition. In the existing literature, considerable research has been dedicated to Ni-based catalysts supported on Al_2O_3 in the context of CO_2 methanation.[2,5–10] Such systems offer substantial activity while being significantly more cost-effective than catalysts based on noble metals like Rh and Ru.[11,12] However, these catalysts are still prone to coke deposition and sintering under the reaction conditions. Hence, the quest for a suitable catalyst for CO_2 methanation continues, with investigations focused on selecting the appropriate support, active phase, promoter, as well as refining the preparation method and reactor design.

The utilization of mixed oxides as catalytic supports is gaining increasing attention due to their ability to exhibit tunable properties and modified metal–support interactions,[13] in addition to the synergetic effect from the individual oxide components.[14] The use of MgO, for instance, is an attractive approach due to its strong basicity that can enhance the adsorption of CO_2 and improve the reaction yield.[15] Enhancing the basicity of the catalysts creates additional adsorption sites for CO_2 and favors the formation of more reactive reaction intermediates.[16] The advantageous promotional effect of introducing Mg to Al_2O_3 on Ni-based[17–19] and Co-based[20] catalytic systems has been established to improve catalyst stability in dry reforming[17,18,20] and combined steam and dry reforming of methane.[19] In CO_2 methanation, research indicates that adding Mg to the Pd/SiO_2 catalyst increased the CO_2 conversion from 40.8 to 59.2% and the CH_4 selectivity from 10.4 to 95.3% at 450 °C.[21] Similarly, co-impregnating Ni and Mg on SiO_2 enabled the catalyst to maintain stability at 67% CO_2 conversion and over 98% CH_4 selectivity for a minimum of 50 hours.[22] Impregnating up to 2.5% of Mg on Ni-based USY zeolites results in 15% and 20% enhancements in CO_2 conversion and CH_4 selectivity, respectively.[23] Likewise, proper Mg loading on Ni-5 Mg/SBA-15-AE sample can efficiently catalyze CO_2 activation,[24] to reach 50% conversion at 295 °C, compared to 315 °C on unpromoted Ni/SBA-15-AE sample. These studies[23,24] suggest that the amount of Mg-loading greatly impacts the extent of CO_2 methanation. In line with these findings, Li *et al.*[25] established an optimal Ni-to-Mg mass ratio of 0.26 for achieving high CO_2 conversion rates. While these studies primarily used Mg as a promoter to enhance the methanation activity, its importance also resides in its use as a catalytic support. In this regard, Julkapli and Bagheri[26] reviewed the use of MgO as a heterogeneous catalyst support and highlighted its capability to modify the acid–base properties of the catalyst, resulting in higher selectivity and lower formation of by-products. However, as a single oxide, MgO shows low thermal stability, particularly in humid and aqueous environments.[26] As a component in mixed oxide supports, Mg plays a vital role in enhancing the basicity of the samples and increasing the metal–support interactions, which reflect in improved catalytic activity, as validated in several applications such as dry reforming of methane,[27,28] hydrotreating,[29] water gas shift,[30] and ethanol coupling reactions.[31] In CO_2 methanation, the presence of Mg^{2+} strong basic sites in Ni/La_2O_3–MgO–CeO_2 enhances the Ni interaction with the support and this emerges as a key factor to achieve high catalytic activity.[32] In a similar context, the improved methanation activity of an MgO-modified ZrO_2 support for Ru-based catalysts is attributed to better active phase dispersion and fast reaction intermediates decomposition and hydrogenation to methane.[33] Likewise, the addition of basic MgO to Al_2O_3 alters the acidity of the catalyst, resulting, for example, in improved reactant conversion to syngas with an absence of carbon deposition during DRM,[27] enhanced sulfidation of CoMo active metals for water gas shift reaction,[30] and boosted ethanol coupling selectivity to butanol.[31] However, most of these studies[28,29,31] use a fixed MgO–Al_2O_3 support with a constant MgO content and evaluate the effects of metal nature, active metal loading, promoter, or calcination temperature. The effect of increasing MgO content in Ni/Al_2O_3 catalysts have been recently evaluated for the dry reforming of methane reaction.[34–36] Results show that the MgO content affects the Ni particles stability and interaction with the support, thus altering the hydrogen yield and carbon deposition. Yet, to the best of our knowledge, the effect of variation of Mg content in MgO–Al_2O_3 supports on CO_2 methanation has not been studied in literature before.

Concerning the active phase, several studies have explored the utilization of cobalt as an alternative for CO_2 methanation,[37–45] primarily due to its activity in Fischer–Tropsch synthesis, with a tendency to generate more methane than heavier hydrocarbons.[46,47] As a result, cobalt has been examined across various oxides and mixed oxide supports, including TiO_2, ZrO_2, Al_2O_3, SiO_2, CeO_2,[37–40] among others. The outcomes of these investigations have demonstrated diversity, dependent upon the specific support nature[38,39] and the preparation method employed.[37] Le *et al.*[39] identified CeO_2 as a suitable support for Co, while Li *et al.*[38] highlighted ZrO_2 as the optimal choice, attributing the observed deactivation on Al_2O_3 to the presence of acid sites on this support. Nonetheless, studies have consistently shown the enhanced catalytic activity of cobalt compared to other metals. Notably, Co/Al_2O_3 exhibited significantly greater activity in CO_2 methanation compared to Ni/Al_2O_3 at GHSV = 16 000 h^{-1}, even at lower metal loading, with the discrepancy attributed to divergent reaction intermediates during the process.[41] The distinct reaction intermediates were also linked to the influence of additives used in conjunction with Co/Al_2O_3 (such as Na, K, Mg, or Ca), leading to varying CH_4 yields in each case.[40] Indeed, while single metal oxide catalysts are subject to poisoning and low thermal stability, the use of multiple oxides can help overcome these problems and achieve enhanced properties, such as better metal dispersion, resulting

in improved catalytic activity.[48] In this regard, Co exhibited superior methanation activity when incorporated alongside Ni on Al_2O_3 support compared to Fe and Mo.[42] This points toward the potential of bimetallic catalysts to enhance catalytic properties through modifications in Ni dispersion, the fundamental characteristics of the support, and the Ni–support interaction.[13,49] For instance, the utilization of Ni–Co supported on $CaAl_2O_4/Al_2O_3$ leads to an enhanced coking resistance during partial methane oxidation.[50] In CO_2 methanation, the bimetallic Ni–Co catalyst supported on ordered mesoporous alumina showed excellent stability at 500 °C for 60 hours, while the Ni-based catalyst exhibited a 14.8% decrease in CO_2 conversion.[51] Nevertheless, the favorable impact of bimetallic Ni–Co catalysts, as reported in certain studies,[51,52] did not manifest evidently in other investigations[53,54] since large metal particles were formed using $Co/Ni/Al_2O_3$ and resulted in lower CH_4 yield, in addition to CO formation.[53] Hasrack *et al.*[54] showed comparable stability at 250 °C for 5 hours, with a slightly higher performance of $1Co15Ni/CeO_2$ catalyst.

Alternatively, an increasing focus has been directed towards incorporating promoters into Ni-based catalysts, aiming to enhance specific properties while benefitting from the accessibility and cost-effectiveness associated with these additives.[55] For example, the addition of strontium (Sr) to $Ni/CeZrO_x$ increased the basicity of the catalyst and resulted in an enhancement of CO_2 adsorption.[56] It also improved the metal–support interaction when used as a promoter on Ni-based catalysts supported on Al_2O_3,[57–59] thus boosting the catalytic performance during CO_2 methanation. The addition of Sr to Ni/SiO_2 catalysts increased CO_2 conversion from 64.7 to 70.5% and CH_4 selectivity from 97.5 to 98.9% at 350 °C and 15 000 ml h^{-1} g^{-1} while preventing Ni metal sintering.[60] Similarly, the utilization of CeO_2 is advantageous owing to its inherent oxygen storage capacity, which can help address the issue of carbon deposition on the catalyst's surface.[61] Cerium introduces oxygen vacancies that can lead to higher conversion of CO to CO_2 during propane steam reforming, for example, preventing carbon deposition and resulting in higher hydrogen production.[62] It has been reported that oxygen defects on the surface of the catalyst play an important role in enhancing CO_2 adsorption, activation, and conversion by hydrogenation into methane.[63] Liu *et al.*[64] revealed an improvement in CO_2 conversion from 45 to 71% upon the addition of 2 wt% CeO_2 to Ni/Al_2O_3 catalyst during CO_2 methanation at 300 °C and 15 000 ml h^{-1} g^{-1}. A higher CeO_2 loading can result in active site coverage and consequent activity loss. Likewise, a 2.5 wt% Ce addition to 10 wt% Ni supported on Al_2O_3 boosted CO_2 conversion from 58 up to 71% and CH_4 selectivity from 94 to 96%, while reducing CO selectivity.[65]

Therefore, it is intriguing to leverage the benefits of each catalyst constituent to achieve superior performance in CO_2 methanation. To the best of our knowledge, only a limited number of studies have explored such intricate combinations. Varbar *et al.*[66] evaluated the effect of Co addition to 20 wt% $Ni/MgAl_2O_4$ in methane oxidation and found that the addition of 3 wt% Co is optimum to limit side reactions. Zhang *et al.*[67] varied the amount of CeO_2 added to $Ni/MgO–Al_2O_3$ in CO methanation and determined an optimum content of 10 wt% CeO_2 for high performance. The use of cobalt-promoted Ni–Mg–Al hydrotalcite-derived catalysts[68] or Co–Ni–Mg–Al mixed-oxides[69] can be promising in CO_2 methanation, yet these studies do not focus on the effect of each component of the catalyst.

Therefore, the innovation intrinsic to our present work resides in the comprehensive assessment of the impact of each catalyst constituent. While limited literature evaluates the composition of mixed-oxide support,[34–36] we assess in this work the increase of Mg-content in $MgO–Al_2O_3$ support and its effect on catalyst basicity and resulting activity in CO_2 methanation. Furthermore, the preceding literature shows that cobalt can be a potential active phase for CO_2 methanation and methane production, yet its performance depends on the nature of support and the type of promoters along which it is tested. This is due to different surface properties such as the interaction of the metal with its support, its dispersion, reducibility, and basicity. It is thus suggested in this work to test this candidate along with nickel on an optimized $MgO–Al_2O_3$ support. While the effect of using Ni- and/or Co-based catalysts vary from one study to another, the effect of mono- and bi-metallic catalysts and the possible synergetic effect between the two metals will be explored on the best $MgO–Al_2O_3$ support. Also, on these samples, we additionally explore possible benefits from incorporating suitable promoters for CO_2 methanation: Sr will be added as a promoter to enhance catalyst basicity, while Ce will be tested in this composition to improve metal dispersion and metal oxides reducibility and overcome carbon deposition problems. These enhancements are expected to improve the catalytic performance during CO_2 methanation. Such promising combinations have not been tested for CO_2 methanation before.

Experimental

Catalyst preparation

The supports used in this work were obtained as a gift from SASOL Anckelmannsplatz 1, 20537, Hamburg, Germany. As specialized providers of alumina-based catalyst carriers, they offered these supports to be used and tested in CO_2 methanation, among other catalytic applications. They were composed of different alumina and magnesium oxide ratios, specifically including 20, 30, 63, and 70 wt% MgO balanced with Al_2O_3. The catalysts were prepared *via* the impregnation method. For the first series of samples, 20 mL of distilled water and the appropriate amount of nickel nitrate hexahydrate [$Ni(NO_3)_2{\cdot}6H_2O$, 98%, Alfa Aesar] to get 5.0 wt% loading of nickel oxide and the required amount of support (mixture of alumina and magnesium oxide) were mixed and stirred at room temperature in a crucible. After 30 minutes, the solution was dried while being stirred at 80 °C. The catalysts were then calcined at 600 °C for 3 hours. The resulting samples are denoted Ni_5/Mg_xAl_{100-x} (x = 20, 30, 63, or 70 wt%).

For the second series of samples, the corresponding amount of $Ni(NO_3)_2{\cdot}6H_2O$ and/or $Co(NO_3)_2{\cdot}6H_2O$ to get 5.0 wt% Co or 2.5% Ni + 2.5% Co was dissolved in 30 ml of distilled water with stirring and heating. Afterwards, 63% MgO and 37% Al_2O_3 support were added, and the stirring was continued for 30 minutes. The obtained catalysts were dried at 120 °C for 20 hours and then calcined for 5 hours at 600 °C. The promoted catalysts were prepared by incorporating 3 wt% of either Ce or Sr along the active metals before the support addition stage, using their corresponding nitrates ($Ce(NO_3)_3{\cdot}6H_2O$; $Sr(NO_3)_2$). The resulting samples are referred to as $Co_5/Mg_{63}Al_{37}$ (Ni-free sample), $Ni_{2.5}Co_{2.5}/Mg_{63}Al_{37}$, $Ni_{2.5}Co_{2.5}Ce_3/Mg_{63}Al_{37}$ or $Ni_{2.5}Co_{2.5}Sr_3/Mg_{63}Al_{37}$.

Catalyst characterization

The textural properties of the samples were evaluated using a Micromeritics Tristar II 3020 surface area and porosity analyzer after degassing at 200 °C for 3 h using N_2. The XRD data were recorded on a Rigaku (Miniflex) diffractometer equipped with Cu Kα radiation and operated at 40 kV and 40 mA. The diffractograms were collected in a 2θ range between 5 and 90° at a step 0.02°. The Diffrac. EVA v4.2.1 software was used to identify the crystallite species present and estimate their size. The temperature-programmed desorption (TPD) data were acquired using Micromeritics Auto Chem II 2920, after running 30 ml min^{-1} of a 10% CO_2/He mixture over the sample for 30 minutes at 50 °C. Then, the temperature increased to 900 °C, and the amount of CO_2 desorbed was found at various temperatures using a TCD detector. The total amount of CO_2 desorbed was thus calculated by integration of the resulting peaks. The FTIR data were taken using a Perkin Elmer GX spectrophotometer. The spectra were registered at the range 400–4000 cm^{-1} employing a KBr pellet. The TEM images were obtained using a transmission electron microscope JEOL JEM-2100F, USA, operated at 120 kV. A laser Raman (NMR-4500) spectrometer (JASCO, Japan) was employed to collect the Raman spectra of the spent catalysts using an objective lens of 100× magnification. The excitation beam was fixed at 532 nm wavelength, and the laser intensity was set at 1.6 mW for a 10-second exposure time at 3 accumulations. A Micromeritics Auto-Chem II 2920 device was used to perform H_2 temperature-programmed reduction (H_2-TPR). The catalyst sample was heated for one hour at 200 °C in an argon environment prior to the measurements, and it was then cooled to room temperature. Using a gas mixture of H_2/Ar (v/v, 10/90) at a flow rate of 40 mL min^{-1}, 0.07 g of the sample was heated at a rate of 10 °C min^{-1} to 1000 °C. The H_2 consumption was captured using a TCD detector.

Catalyst testing

The catalytic activity was evaluated in a fixed-bed stainless-steel continuous-flow reactor (PID Eng. & Tech), having an internal diameter of 0.94 cm and a length of 30 cm. The reaction temperature was controlled and monitored by using a thermocouple placed in the center of the catalytic bed. A schematic of the reaction setup is shown in Fig. 1. At the beginning of the test, 0.12 g of each sample was first reduced *in situ* under a hydrogen flow of 30 mL min^{-1} at 800 °C for 2 hours at atmospheric pressure. Then, the reactor was cooled, and a total reactive flow of 30 mL min^{-1}, composed of 16 mL min^{-1} H_2, 4 mL min^{-1} CO_2 and 10 mL min^{-1} N_2, was introduced at an equivalent gas hourly space velocity (GHSV) of 15 000 mL h^{-1} g_{cat}^{-1}. The mixture was carried by argon gas in a gas chromatograph (GC). The methanation reaction was performed at 400 °C for 300 minutes at atmospheric pressure. The reaction temperature, pressure, and other variables were monitored through the reactor panel. A SHIMADZU GC-2014 equipped with Porapak Q and Molecular Sieve 5A columns and a thermal conductivity detector analyzed the reaction products and feed using a combination of series and bypass connections. To quantify the results from catalytic experiments, the peak areas of the components separated by the GC were analyzed. These peak areas are proportional to the amount of each component present. While a basic comparison can be done using peak areas alone, a calibration process with standard gases is usually employed for more accurate quantification. This involves running known concentrations of reactants and products (external standards) through the GC to create a calibration curve. The peak areas of the samples are then compared to this curve to determine their actual concentrations. Additionally, an internal standard gas (such as N_2) can be added to both samples and calibration standards. By comparing the peak area ratio of the target component to the internal standard, variations in injection volume and detector response are accounted for, leading to more reliable results. The catalytic tests were repeated twice for all the catalysts for reproducibility.

The CO_2 conversion and CH_4 yield were evaluated using eqn (10) and (11):

$$CO_2\ \text{conversion}\ (\%) = \frac{CO_{2\ in} - CO_{2\ out}}{CO_{2\ in}} \times 100 \qquad (10)$$

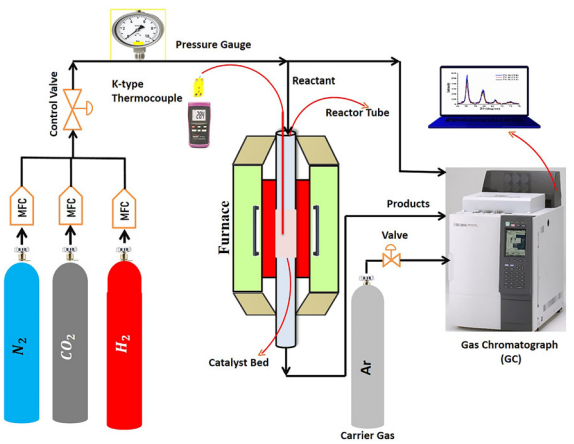

Fig. 1 Reaction setup for the CO_2 methanation testing.

$$\text{CH}_4\text{ yield }(\%) = \frac{\text{CH}_{4\text{ out}}}{\text{CO}_{2\text{ in}}} \times 100 \quad (11)$$

Results and discussion

During CO_2 methanation, the presence of metallic Ni^0 sites is highly essential since they constitute the active sites that promote the adsorption and dissociation of H_2.[6,11,70] Consequently, a reduction step is systematically applied, prior to the methanation reaction to convert nickel oxide into metallic nickel.[57] For these reasons, the samples are examined in this work in their reduced states to understand their properties. Hence, only the textural properties of the calcined samples are shown, while the remaining characterization results of the BET, XRD, CO_2-TPD and FTIR experiments are presented for the samples in their reduced states.

Effect of support composition on CO_2 methanation performance

All the calcined[34,35] and reduced samples exhibited type IV N_2 sorption isotherms (Fig. 2), characteristic of mesoporous materials, comparable to those reported for similar MgO–Al_2O_3 mixed oxide supports.[31] The H4 hysteresis loop observed for all samples is the consequence of MgO presence in the samples.[28] The analysis of textural properties (Table 1) indicated a gradual decline in surface area and pore volume with the increase in the percentage of MgO. Specifically, the BET surface area and pore volume decreased from 184 $m^2\ g^{-1}$ and 0.53 $cm^3\ g^{-1}$ for the reduced $Ni_5/Mg_{20}Al_{80}$ to around 197 $m^2\ g^{-1}$ and 0.29 $cm^3\ g^{-1}$ for reduced $Ni_5/Mg_{63}Al_{37}$ and 161.2 $m^2\ g^{-1}$ and 0.27 $cm^3\ g^{-1}$ for reduced $Ni_5/Mg_{70}Al_{30}$, respectively. This can be explained by possible pore blockage as the MgO content increases in the support.[35] Furthermore, a similar trend was observed for the pore size, which dropped from 8.4 nm for reduced $Ni_5/Mg_{20}Al_{80}$ to approximately 5.5 nm for reduced $Ni_5/Mg_{63}Al_{37}$. This is attributed to the presence of more Mg species in the pores, as also observed in Mg-containing Ni/SBA-15 catalytic systems.[24]

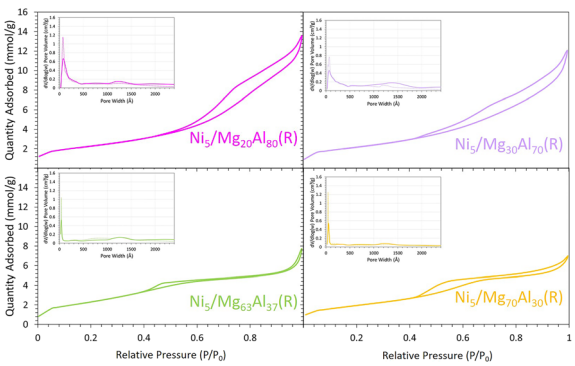

Fig. 2 N_2 sorption isotherms and pore size distribution (inset figures, solid line: adsorption, dashed line: desorption) for the reduced Ni_5/Mg_xAl_{100-x} (where x = 20, 30, 63 or 70 wt%) samples.

The H_2-TPR profiles, reported in previous studies,[34,35] exhibit a prominent reduction peak ranging from 700 to 1000 °C. This indicates two important points: firstly, the absence of free NiO species that are typically reduced between 300 and 400 °C;[15] and secondly, the positioning of this peak at 830, 840, 860, and 925 °C for an Mg content of 20, 30, 63 and 70%, respectively. This implies that an increase in the Mg content of the support delays the reduction process and makes the reducibility of the active phase more difficult. This phenomenon is commonly attributed to the formation of either a stable NiO–MgO solid solution,[15,23] or $MgNiO_2$ (ref. 24) upon the incorporation of Mg, suggesting a strong interaction between NiO and MgO in both cases. In this regard, Kumar *et al.*[29] reported stronger metal–support interaction of Mo/MgO–Al_2O_3 compared to single oxide supports. Similarly, Lian *et al.*[30] reported a higher metal–support interaction upon the increase in Mg content in Co–Mo/MgO–Al_2O_3 samples. Furthermore, during the reduction, hydrogen consumption rises proportionally with the increment in Mg content. Specifically, it increases from 0.96 mmol g^{-1} for $Ni_5/Mg_{20}Al_{80}$ and $Ni_5/Mg_{30}Al_{70}$ samples to about 1.22 mmol g^{-1} for $Ni_5/Mg_{63}Al_{37}$ and $Ni_5/Mg_{70}Al_{30}$ samples.

Following reduction, the X-ray diffractograms of the reduced samples (Fig. 3) exhibit prominent peaks at about 37, 43, and 63°, which can be primarily attributed to magnesium nickel oxide $Mg_{0.7}Ni_{0.3}O$ (ref. 04-023-4643) or MgO (ref. 00-003-0998), both having a $Fm\bar{3}m$ cubic lattice, corresponding to characteristic interplanar spacings (111), (200) and (220), respectively. These peaks can also be assigned to spinel $MgAl_2O_4$ (ref. 00-005-0672) having a $Fd\bar{3}m$ structure, indexed as (311), (400) and (440), respectively. A more detailed examination of the significant peak unveils a shift towards spinel $MgAl_2O_4$ (~44.8°) at low Mg content and a shift towards MgO (~43.1°) at high Mg content.[15,23] This observation supports the earlier discussion on the formation of a mixed NiO–MgO phase at elevated Mg content, as evident from the TPR results. Moreover, it is in full agreement with published data that show a reduction of the spinel formation upon the increment of Mg content due to the promotion of the mixed solid phase.[15,23,27,28] On these profiles, the presence of very small peaks at 51 and 75° confirms the presence of metallic Ni^0 species.

Furthermore, the assessment of the crystalline domains using the major peak at 43° indicates an increase in their sizes from 4.9 and 4.6 nm for $Ni_5/Mg_{20}Al_{80}$ and $Ni_5/Mg_{30}Al_{70}$ reduced samples, respectively, to 5.8 nm for $Ni_5/Mg_{63}Al_{37}$ and 6.9 nm for $Ni_5/Mg_{70}Al_{30}$ reduced samples. This suggests that the increase in Mg content slightly reduces the dispersion of the active phase, as similarly observed in other studies.[18,25] For instance, Karam *et al.*[18] reported an increase in the NiO crystalline domain size from 4.6 nm for Ni_6–Mg_5–Al_2O_3 to 5.4 and 7.7 nm for Ni_6–Mg_{15}–Al_2O_3 and Ni_6–Mg_{26}–Al_2O_3, respectively. Conversely, in Mg-modified Ni/SiO_2 catalysts, an increase in Mg-loading led to improved metal dispersion.[22] This discrepancy can be attributed to different preparation methods employed in each study.

Table 1 Textural properties of the reduced catalysts

Sample	BET surface area ($m^2\ g^{-1}$)	BJH adsorption cumulative pore volume ($cm^3\ g^{-1}$)	BJH desorption cumulative pore volume ($cm^3\ g^{-1}$)	BJH adsorption average pore width (Å)	BJH desorption average pore width (Å)
$Ni_5/Mg_{20}Al_{80}$(R)	183.7	0.49	0.53	94	84
$Ni_5/Mg_{30}Al_{70}$(R)	176.5	0.44	0.47	91	80
$Ni_5/Mg_{63}Al_{37}$(R)	197.3	0.29	0.29	53	55
$Ni_5/Mg_{70}Al_{30}$(R)	161.2	0.25	0.27	58	55
$Co_5/Mg_{63}Al_{37}$(R)	185.3	0.28	0.29	58	57
$Ni_{2.5}Co_{2.5}/Mg_{63}Al_{37}$(R)	212.3	0.30	0.31	52	55
$Ni_{2.5}Co_{2.5}Sr_3/Mg_{63}Al_{37}$(R)	182.3	0.29	0.29	57	59
$Ni_{2.5}Co_{2.5}Ce_3/Mg_{63}Al_{37}$(R)	175.7	0.27	0.29	56	60

The evaluation of the basicity of the reduced samples is conducted using CO_2-TPD (Fig. 4). The resulting peaks can be conventionally decomposed into three major regions: the 50 to 200 °C range for low basicity, 200 to 400 °C for moderate basicity, and above 400 °C for strong basicity.[57] Irrespective of the Mg content, all peaks are predominantly centered around 250 °C, indicating the presence of mainly moderate basic sites on all samples. Notably, the $Ni_5/Mg_{63}Al_{37}$ sample displays the highest amount of desorbed CO_2 of 0.29 mmol g^{-1}, in contrast to the values of 0.11, 0.16, and 0.22 mmol g^{-1} for $Ni_5/Mg_{20}Al_{80}$, $Ni_5/Mg_{30}Al_{70}$ and $Ni_5/Mg_{70}Al_{30}$, respectively. Comparably, the total basicity of catalysts increased with increasing Mg content from 0.32 μmol m^{-2} for Ni–3Mg/SBA-15-WI to 0.39 and 0.41 μmol m^{-2} for Ni–5Mg/SBA-15-WI and Ni–7Mg/SBA-15-WI, respectivel.[24] Similarly, the total amount of CO_2 desorbed increased from 1.84 mmol g^{-1} to 5.19 mmol g^{-1} as the Mg/Al ratio of the support increased from 0.3 to 2.[27] This implies that the magnitude of Mg loading substantially influences the extent of CO_2 adsorption on the catalyst, consequently impacting the catalytic performance, a topic that will be elaborated on in the subsequent section.

The FTIR results (Fig. 5) reveal transmission bands at 3430 and 1630 cm^{-1} that can be assigned to stretching and bending vibrations of –OH hydroxyl groups or adsorbed water on the surface of the samples, respectively.[70,71] The transmission bands at 2890 and 2350 cm^{-1} are attributed to –C–H stretch,[58] and to CO_2 adsorption on the samples,[72] respectively. The bands between 400 and 500 cm^{-1} correspond to Ni–O stretching[73] and Ni–O–Ni bond.[74]

The CO_2 methanation performance of the reduced samples is evaluated at 400 °C (Fig. 6). Overall, all samples exhibit stability and maintain a constant level of CO_2 conversion and CH_4 yield for about 300 min. This finding aligns with previous research,[75] which suggests that the presence of medium basic sites facilitates the hydrogenation step and enhances CO_2 methanation.

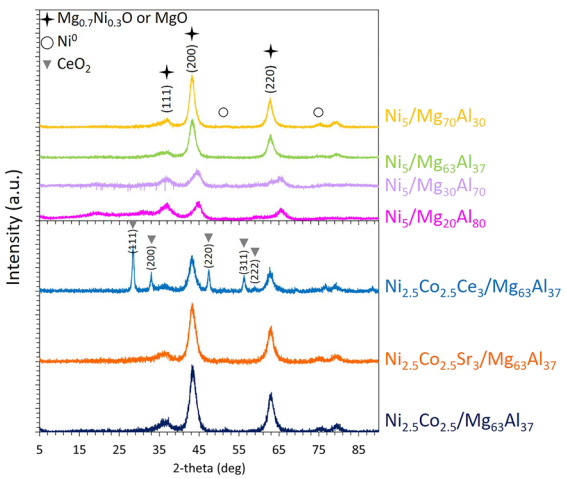

Fig. 3 XRD patterns of the reduced Ni_5/Mg_xAl_{100-x} (where x = 20, 30, 63, or 70 wt%) catalysts and Co-containing catalysts supported on $Mg_{63}Al_{37}$, along with the characteristic (*hkl*) interplanar planes of the identified species.

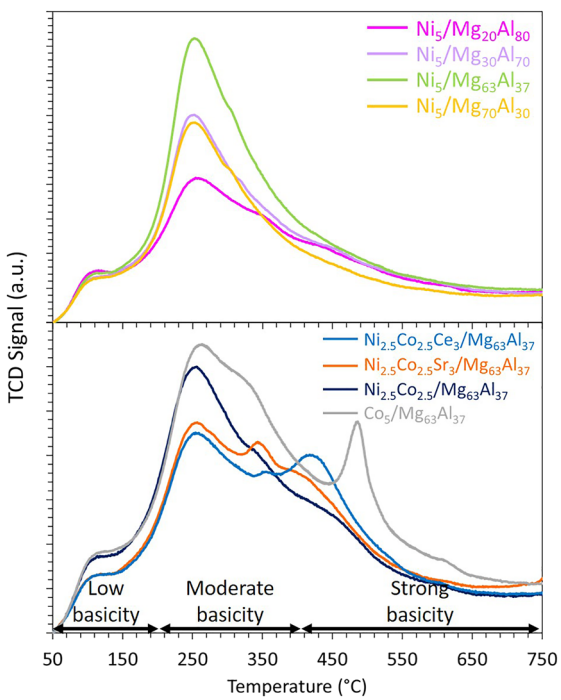

Fig. 4 CO_2-TPD results of reduced Ni_5/Mg_xAl_{100-x} (where x = 20, 30, 63 or 70 wt%) catalysts and Co-containing catalysts supported on $Mg_{63}Al_{37}$.

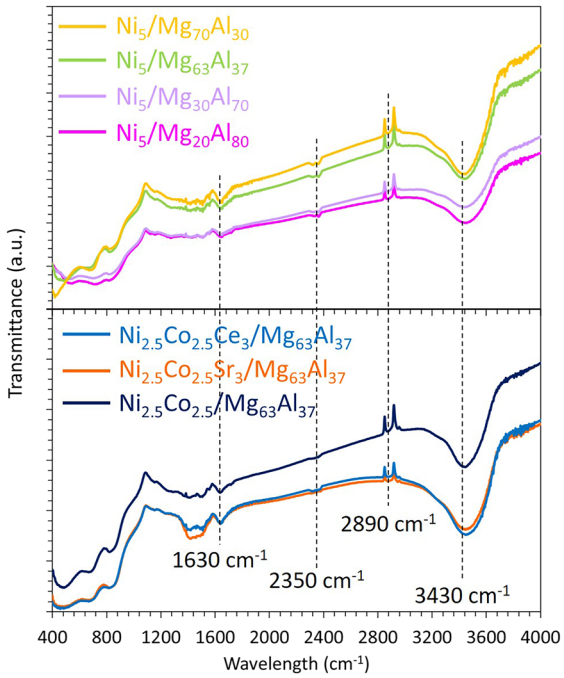

Fig. 5 FTIR spectra of the reduced Ni_5/Mg_xAl_{100-x} (where x = 20, 30, 63 or 70 wt%) catalysts and Co-containing catalysts supported on $Mg_{63}Al_{37}$.

In more specific terms, the CO_2 conversions are approximately 83% for $Ni_5/Mg_{20}Al_{80}$, 89% for $Ni_5/Mg_{30}Al_{70}$, 92% for $Ni_5/Mg_{63}Al_{37}$ and 90% for $Ni_5/Mg_{70}Al_{30}$. Notably, the $Ni_5/Mg_{30}Al_{70}$ catalyst demonstrates the highest CO_2 conversion, while the $Ni_5/Mg_{20}Al_{80}$ catalyst exhibits the lowest activity. The trend in CO_2 conversion seems to align with the amount of CO_2 desorbed during the CO_2-TPD experiment (Fig. 8). This suggests that the catalyst with the strongest affinity for CO_2 displays the highest activity during the reaction.

However, despite the $Ni_5/Mg_{70}Al_{30}$ sample showing relatively high CO_2 conversion, it is the least selective and produces the lowest CH_4 yield. Indeed, the CH_4 yield changes as follows: $Ni_5/Mg_{70}Al_{30}$ (75%) < $Ni_5/Mg_{20}Al_{80}$ (78%) < $Ni_5/Mg_{30}Al_{70}$ (80%) < $Ni_5/Mg_{63}Al_{37}$ (82%). These findings imply that increased Mg content enhances the catalytic activity by improving both CO_2 conversion and CH_4 yield. Nevertheless, an optimal Mg content of 63% seems to strike a balance, as further increase negatively impacts catalytic performance, leading to a significant drop in both CO_2 conversion and CH_4 yield. Similar findings were also obtained on Ni–Mg_x/coconut shell carbon (CSC) catalysts,[25] where the high performance of the optimum catalyst (x = 0.26) was assigned to its strong basicity and strong adsorption affinity for CO_2.

Interestingly, the XRD profiles of the $Ni_5/Mg_{63}Al_{37}$ catalyst before and after testing (Fig. 7a and a′) show preservation of the peaks and their relative intensities, as observed on the reduced sample earlier. This indicates the absence of metal sintering and the preservation of a good active phase dispersion throughout the test. On the Raman spectra (Fig. 7b), the absence of the G-band at around 1580 cm^{-1} and the D-band near 1350 cm^{-1}, typical of carbon-containing materials, reveals the absence of carbon deposition on the used $Ni_5/Mg_{63}Al_{37}$ catalyst. These observations are also validated on the TEM images of the $Ni_5/Mg_{63}Al_{37}$ catalyst before and after testing (Fig. 7c and c′) that confirm the absence of carbon deposits and show good maintenance of active phase dispersion without apparent metal agglomeration, suggesting high thermal stability of the sample under the employed conditions.

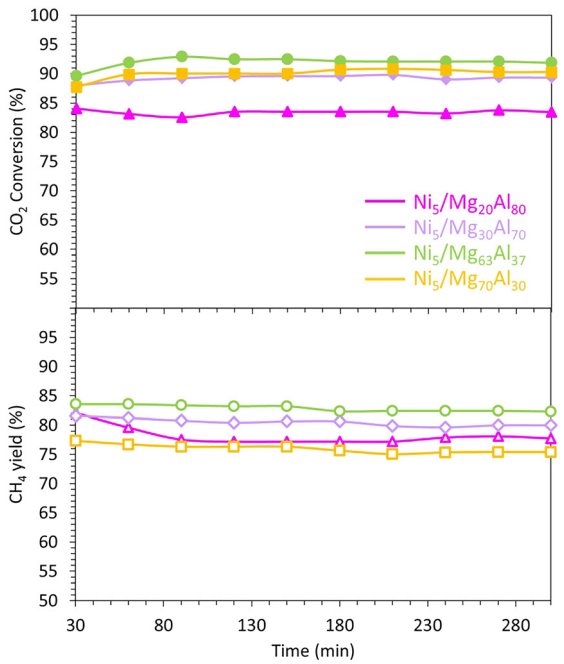

Fig. 6 Catalytic test results of the Ni_5/Mg_xAl_{100-x} (where x = 20, 30, 63 or 70 wt%) catalysts. The methanation reaction was performed at 400 °C for 300 minutes, at an equivalent gas hourly space velocity of 15 000 mL g^{-1} h^{-1}.

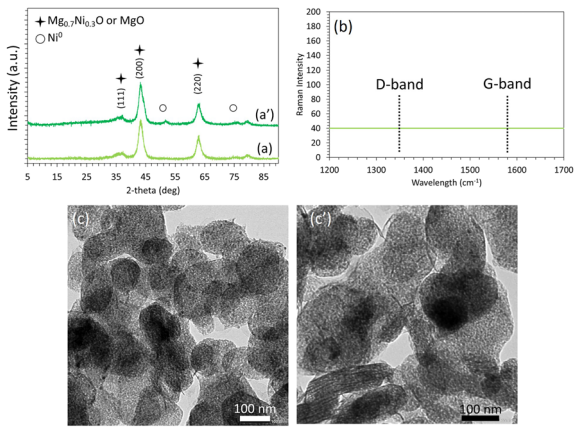

Fig. 7 XRD profiles (a and a′), Raman spectra (b) and TEM images (c and c′) of the reduced (a and c) and spent (a′, b and c′) $Ni_5/Mg_{63}Al_{37}$ catalysts.

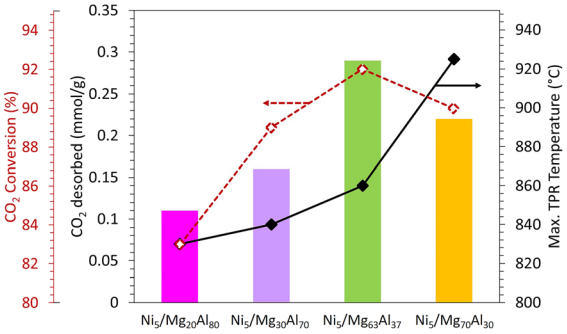

Fig. 8 Amount of CO_2 desorbed by CO_2-TPD (mmol g^{-1}), CO_2 conversion (%) and maximum TPR temperature (°C) obtained on Ni_5/Mg_xAl_{100-x} (where x = 20, 30, 63 or 70 wt%) catalysts.

To better clarify the effect of Mg loading on the catalytic performance, the catalytic test results are coupled with the amount of CO_2 desorbed during CO_2-TPD and the maximum reduction temperature observed during TPR (Fig. 8). The results illustrate that the extent of CO_2 conversion (shown in red in Fig. 8) follows the same pattern as the amount of CO_2 desorbed during CO_2-TPD (depicted as a histogram in Fig. 8). CO_2 conversion increases with the increase in Mg content up to 63 wt% and then declines beyond this threshold, aligning with the trend observed in the amount of CO_2 desorbed during CO_2-TPD. This suggests that the most active catalyst, namely $Ni_5/Mg_{63}Al_{37}$ sample, exhibits the highest CO_2 desorption, signifying the highest CO_2 adsorption affinity. Moreover, the NiO reduction occurs at a reasonable temperature (black curve in Fig. 8). Consequently, the Mg_{63}-Al_{37} support is chosen for further investigation in the subsequent phases of the study.

The absence of similar catalysts tested in literature for CO_2 methanation makes the comparison of performance challenging. While the 5Ni–7Mg–Al_2O_3 and 5Ni–26Mg–Al_2O_3 show compositions close to the samples used in this work,[15] they present lower conversions than those of the current study. This can be primarily attributed to the much higher gas hourly space velocity of 86 100 mL g^{-1} h^{-1} used during the test[15] compared to 15 000 mL g^{-1} h^{-1} applied in the present work. Thus, differences in the operating conditions can make the catalytic comparison impractical. Yet, the optimum properties discussed above and the superior catalytic performance of the $Ni_5/Mg_{63}Al_{37}$ catalyst reflect in higher performance compared to some catalytic systems reported in the literature (Table 2). Indeed, at the same reaction temperature of 400 °C, the CO_2 conversion of the mentioned catalyst is higher than that of 30Ni/Al_2O_3·0.5SiO_2 (ref. 14) and other Ni–Mg_x samples supported on coconut shell carbon (CSC),[25] even when the latter are tested at lower GHSV. The samples presented in this work are tested under more drastic conditions, *i.e.* higher GHSV of 15 000 mL g^{-1} h^{-1}, yet they still show higher performance than those tested under milder conditions using a GHSV of 9000 and 10 000 mL g^{-1} h^{-1}. Such differences can be associated with variations in catalyst composition or differences in the preparation methods adopted in each study. In this regard, Burger *et al.*[76] showed that employing different preparation methods for Ni–Al catalysts can result in completely different chemical interactions that translate into diverse behaviors in CO_2 methanation upon Fe-doping. In more detail, the large difference between the CO_2 conversion obtained in this work and that of 30Ni/Al_2O_3·0.5SiO_2 can be assigned to the absence of MgO, and consequently of basic sites, on the sample, limiting thus CO_2 adsorption and conversion. More globally, an evaluation of the TPR profiles of the various samples compared in Table 2 reveals that most of these samples are reducible at temperatures near 700 °C, which are much lower than that of $Ni_5/Mg_{63}Al_{37}$ (860 °C). This implies that higher metal–support interactions are achieved on $Ni_5/Mg_{63}Al_{37}$, reflecting in higher catalytic performance. This comparison highlights the beneficial effect of using MgO–Al_2O_3 in optimized proportions as a catalytic support for Ni-based samples in CO_2 methanation.

Effect of the bimetallic catalyst

On the $Mg_{63}Al_{37}$ support, the use of monometallic Co and bimetallic Ni–Co active phases is investigated. The properties of the reduced samples are first evaluated. While the monometallic and bimetallic samples demonstrate comparable textural properties (Fig. 9 and Table 1) and exhibit identical particle size in the range of 5.7–5.8 nm based on the XRD data (Fig. 3), the TPR (Fig. 10) and CO_2-TPD (Fig. 4) results present distinct differences.

To elaborate, the reduction of the $Co_5/Mg_{63}Al_{37}$ sample shows two major reduction peaks at around 340 and 930 °C. These peaks correspond to the reduction of Co_3O_4 to CoO and

Table 2 Comparison of CO_2 conversion at 400 °C in literature with the current work

Sample	Catalyst weight (mg)	Reaction temperature (°C)	$H_2:CO_2$	GHSV (mL g^{-1} h^{-1})	CO_2 conversion (%)	Ref.
$Ni_5/Mg_{63}Al_{37}$	120	400	4	15 000	92	This study
5Ni–7Mg–Al_2O_3	200	400	4	89 400	60	15
5Ni–26Mg–Al_2O_3					65	
30Ni/Al_2O_3·0.5SiO_2	200	400	3.5	9000	72	14
Ni–$Mg_{0.13}$/CSC	300	400	4	10 000	80	25
Ni–$Mg_{0.26}$/CSC					88	
Ni–$Mg_{0.39}$/CSC					85	

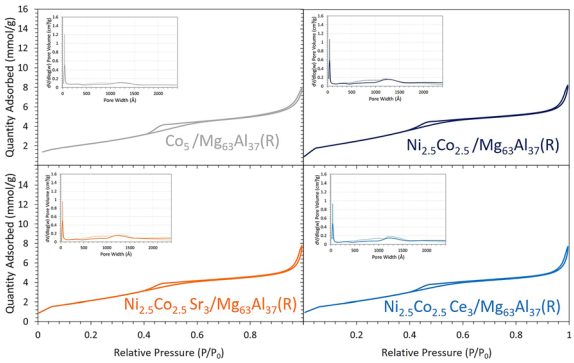

Fig. 9 N_2 sorption isotherms and pore size distribution (inset figures, solid line: adsorption, dashed line: desorption) for the reduced Co-containing catalysts supported on $Mg_{63}Al_{37}$.

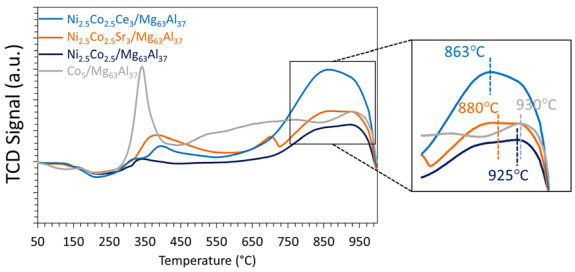

Fig. 10 H_2-TPR profiles of Co-containing catalysts supported on $Mg_{63}Al_{37}$.

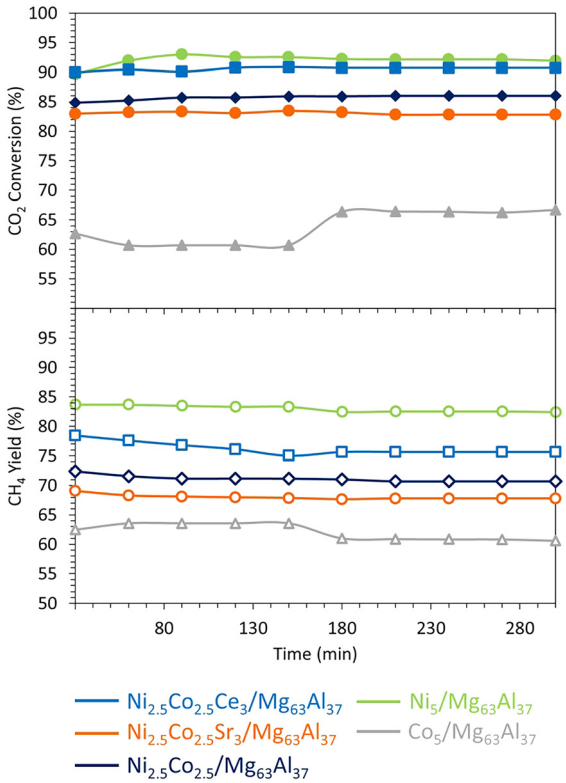

Fig. 11 Catalytic test results of the Co-containing catalysts supported on $Mg_{63}Al_{37}$. The methanation reaction was performed at 400 °C for 300 minutes, at an equivalent gas hourly space velocity of 15 000 mL g^{-1} h^{-1}.

subsequently to metallic cobalt.[44] Similarly, the reduction of the bimetallic $Ni_{2.5}Co_{2.5}/Mg_{63}Al_{37}$ sample requires elevated temperatures for complete reduction, with the primary reduction peak centered at 925 °C, as also reported elsewhere.[36] This indicates that the introduction of Co leads to a stronger metal–support interaction, a phenomenon observed in previous studies.[51] It is worth noting that the monometallic Ni-based sample demonstrates the easiest reduction, with a peak observed at 860 °C, as discussed earlier.

The XRD patterns of the Co-containing samples is comparable to those of the Co-free samples (Fig. 3), with an absence of clear peaks characteristic of either Co_3O_4 or metallic Co.[62] This can be attributed to the low Co-content used in these samples or to a high dispersion of small Co particles that cannot be detected by XRD.

The CO_2-TPD results (Fig. 4) indicate that the addition of cobalt contributes to the enhancement of basicity. This is evident as the $Co_5/Mg_{63}Al_{37}$ sample exhibits a distinct peak at approximately 490 °C, indicating the presence of strong basic sites within this sample. Indeed, Alabi *et al.*[28] reported the formation of a stronger basic site on Co catalysts supported on Mg–Al compared to Ni catalysts and assigned this to stronger metal–support interaction. On the bi-metallic $Ni_{2.5}Co_{2.5}/Mg_{63}Al_{37}$ sample, an additional peak is observed at around 450 °C, suggesting a boost of the basicity compared to the mono-metallic Ni-based sample. However, when interpreting these observations in relation to the catalytic test results, it becomes evident that the basicity of the catalyst is not the sole factor influencing the catalytic performance during CO_2 methanation. The nature of the active phase, as well as the ease of reduction, are also crucial parameters contributing to the attainment of a catalyst that is both highly active and stable.

On the $Mg_{63}Al_{37}$ support, the use of Co and Ni–Co active phases is investigated during the methanation reaction at 400 °C and 15 000 mL g^{-1} h^{-1} (Fig. 11). The initial CO_2 conversion recorded is as follows: $Ni_5/Mg_{63}Al_{37}$ (90%) > $Ni_{2.5}Co_{2.5}/Mg_{63}Al_{37}$ (85%) > $Co_5/Mg_{63}Al_{37}$ (63%). The CH_4 yield follows the same trend: $Ni_5/Mg_{63}Al_{37}$ (84%) > $Ni_{2.5}Co_{2.5}/Mg_{63}Al_{37}$ (72%) > $Co_5/Mg_{63}Al_{37}$ (63%). Consequently, the catalytic activity seems to be affected by the type of active phase employed since the Co-based catalyst shows lower catalytic performance compared to the Ni-based one. This result does not agree with the findings of Liang *et al.*,[41] where the Co-based catalyst supported on Al_2O_3 showed higher activity and better stability than the Ni-based one under comparable operating conditions at 400 °C. In this case, the discrepancy can be essentially related to the different nature of the support (MgO–Al_2O_3 mixed oxide) employed in this study. After 150 min on stream, the $Co_5/Mg_{63}Al_{37}$ sample reveals a rise in CO_2 conversion from 63% up to 67%, accompanied by a decrease in CH_4 yield from 63% to 61%. This increase in CO_2 conversion can be due to the occurrence of side

reactions such as RWGS (eqn (2)), DRM (eqn (3)), or reactions that generate solid carbon (eqn (5) and (6)). At the reaction temperature of 400 °C, the change in Gibbs free energy ΔG is 13.965 kJ for eqn (2), 68.319 kJ for eqn (3), −25.127 kJ for eqn (5), and −9.864 kJ for eqn (6). Consequently, the first two reactions (eqn (2) and (3)) are not favorable under the reaction conditions ($\Delta G > 0$ at 400 °C), then it is more likely that the increase in CO_2 conversion and decrease in CH_4 yield is due to the simultaneous occurrence of eqn (5) and (6) that consume CO_2 and result in solid carbon on the surface of the catalyst. This effect is alleviated upon the use of bimetallic catalysts since the $Ni_{2.5}Co_{2.5}/Mg_{63}Al_{37}$ sample maintains a constant level of activity throughout the test. Notably, the bimetallic Ni–Co catalyst prepared with the optimal support demonstrates superior performance compared to analogous catalytic systems tested in the literature on different supports, even with higher active phase loadings. For instance, while $Ni_{2.5}Co_{2.5}/Mg_{63}Al_{37}$ achieved about 85% CO_2 conversion at 400 °C and 15 000 mL g^{-1} h^{-1}, a 30Ni–5Co/Al_2O_3 sample reaches no more than 65% CO_2 conversion under the same test conditions, despite a lower GHSV of 9000 mL g^{-1} h^{-1}.[55] Likewise, the utilization of 15Ni–12.5Co on Al_2O_3 support attains a maximum of 45% CO_2 conversion at 300 °C and 9000 mL g^{-1} h^{-1}.[52] These findings underscore the significance of optimizing the catalytic support to achieve high performance in CO_2 methanation.

Effect of Ce and Sr promoters

Subsequently, to improve the catalytic performance of the bimetallic $Ni_{2.5}Co_{2.5}/Mg_{63}Al_{37}$ sample, the latter is promoted with either Sr or Ce. The promoted samples present a type IV isotherm (Fig. 9), characteristic of mesoporous materials. The BET surface area for all reduced samples falls within the range of 176 to 212 m^2 g^{-1} with a pore volume of about 0.3 cm^3 g^{-1} and a pore size in the range of 5.5–6.0 nm (Table 1). These textural properties are similar to those of the bimetallic $Ni_{2.5}Co_{2.5}/Mg_{63}Al_{37}$ sample.

The TPR profiles of the promoted samples (Fig. 10) show a minor reduction peak at around 400 °C, attributed to cobalt oxide reduction, and a second more pronounced peak, above 800 °C, attributable to the reduction of nickel oxide. The maximum of this peak shifts from 925 °C for $Ni_{2.5}Co_{2.5}/Mg_{63}Al_{37}$ to 880 °C for $Ni_{2.5}Co_{2.5}Sr_3/Mg_{63}Al_{37}$ and to 863 °C for $Ni_{2.5}Co_{2.5}Ce_3/Mg_{63}Al_{37}$. Hence, it becomes evident that the incorporation of Ce reduces the reduction temperature, thereby enhancing the reducibility of nickel oxide.

Post-reduction, the XRD results (Fig. 3) indicate consistent major peaks at 37, 43, and 63° previously assigned to $Fm\bar{3}m$ cubic magnesium nickel oxide $Mg_{0.7}Ni_{0.3}O$ (ref. 04-023-4643). In the $Ni_{2.5}Co_{2.5}Ce_3/Mg_{63}Al_{37}$ sample, additional peaks at 28.5, 33, 47.5, 56.5 and 59° correspond to $Fm\bar{3}m$ cerium oxide structure CeO_2 (ref. 04-016-6171). The assessment of the particle size using the most intense peak at about 44° demonstrates a particle size of 5.2 nm for $Ni_{2.5}Co_{2.5}Sr_3/Mg_{63}Al_{37}$ and 6.3 nm for $Ni_{2.5}Co_{2.5}Ce_3/Mg_{63}Al_{37}$.

As previously mentioned, the addition of cobalt improved the Ni-based sample's basicity. The introduction of Ce as a promoter further enhances the basicity, evident from the emergence of a peak at around 425 °C (Fig. 4), indicative of the presence of strong basic sites on $Ni_{2.5}Co_{2.5}Ce_3/Mg_{63}Al_{37}$ sample. Surprisingly, the incorporation of Sr results in moderate basicity, unlike previously reported data,[56] where the addition of 4% Sr to Ni/CeZr samples contributes to the formation of very strong basic sites on the catalyst's surface. This can be due to the nature of support and its interaction with the active metals since the addition of MgO alters the basicity of alumina support, and the effect of Sr addition on the basicity of the sample might be hindered.

The catalytic stability test results at 400 °C (Fig. 11) show an enhancement of the catalytic activity of the $Ni_{2.5}Co_{2.5}/Mg_{63}Al_{37}$ sample upon the addition of Ce. Indeed, the $Ni_{2.5}Co_{2.5}Ce_3/Mg_{63}Al_{37}$ catalyst presents a CO_2 conversion of 90% and a CH_4 yield of 78% that remains constant throughout the test duration. These values are comparable to those of $Ni_5/Mg_{63}Al_{37}$ but higher than those of $Ni_{2.5}Co_{2.5}/Mg_{63}Al_{37}$ catalyst (only 85% CO_2 conversion and 72% CH_4 yield), highlighting the beneficial impact of Ce addition to the Ni–Co bimetallic catalyst.

The promotional effect of Ce is further examined on the TGA curves of the spent catalysts (Fig. 12), since $Ni_{2.5}Co_{2.5}Ce_3/Mg_{63}Al_{37}$ catalyst shows only 6% weight loss compared to about 11% for $Ni_5/Mg_{63}Al_{37}$ and 10% for $Ni_{2.5}Co_{2.5}/Mg_{63}Al_{37}$. On the TGA profiles, the major weight loss before 200 °C corresponds to the removal of water and other chemisorbed species.[35] Additional weight loss between 200 and 500 °C is attributed to the combustion of amorphous carbon and that above this range (>500 °C) results from the oxidation of graphitic carbon.[35] On all the samples, the very limited weight loss up to 500 °C (about 2%) suggests the removal of reactive amorphous carbon.[35] This is also confirmed by the absence of any filamentous carbon nanotubes on the TEM images of the spent $Ni_{2.5}Co_{2.5}Ce_3/Mg_{63}Al_{37}$ (Fig. 13). Furthermore, the highly active and stable $Ni_{2.5}Co_{2.5}Ce_3/Mg_{63}Al_{37}$ and $Ni_5/Mg_{63}Al_{37}$ catalysts maintain good dispersion of the active phase, without apparent metal agglomeration or carbon deposition on their surfaces (Fig. 7 and 13). This

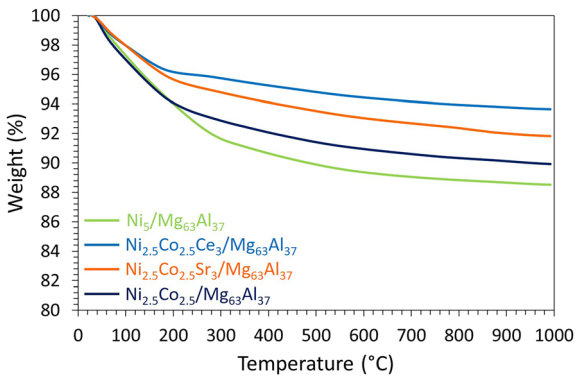

Fig. 12 TGA curves of the spent catalysts supported on $Mg_{63}Al_{37}$.

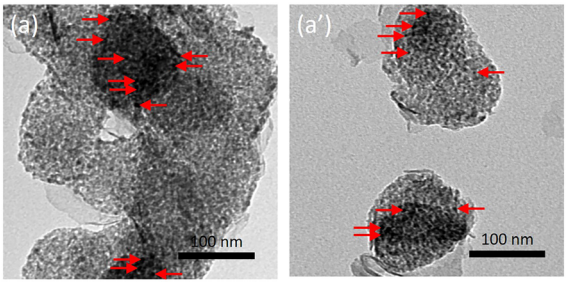

Fig. 13 TEM images of the (a) reduced and (a') spent $Ni_{2.5}Co_{2.5}Ce_3/Mg_{63}Al_{37}$ catalyst.

consistency in active metal dispersion is evident in TEM images before and after the catalytic tests, as indicated by red arrows on Fig. 13, implying the absence of particle sintering and the robust thermal stability of these samples under the employed conditions. The $Ni_{2.5}Co_{2.5}Sr_3/Mg_{63}Al_{37}$ sample, however, exhibits lower catalytic performance compared to the unpromoted sample (83% CO_2 conversion and 69% CH_4 yield). This may arise from the fact that the $MgO–Al_2O_3$ support itself already provides basic sites for CO_2 adsorption, and the Sr loading might not be sufficiently high to significantly enhance basicity beyond what the support itself offers.

The highly performing $Ni_{2.5}Co_{2.5}Ce_3/Mg_{63}Al_{37}$ sample is further examined under the same operating conditions but for longer duration (Fig. 14). It is shown that, after more than 25 hours on stream, this sample maintains high and constant CO_2 conversion of 90% with a stable CH_4 yield at about 75%. After this period, the evaluation of the spent catalyst by TGA shows a limited weight loss that does not exceed 11%. As detailed earlier, the major weight loss of about 7% is assigned to the removal of chemisorbed species and the remaining 4% are primarily assigned to the elimination of amorphous carbon. The XRD profiles present the same characteristic peaks observed on the reduced sample and reveal a preservation of the active sites dispersion with an absence of significant particles sintering. These results confirm, once again, the beneficial effect of Ce addition to the bimetallic Ni–Co catalyst that leads to superior catalytic activity through the enhancement of NiO reducibility and the improvement of basicity. The promotional effect of ceria is comparable to that observed on $Ni/MgO–Al_2O_3–CeO_2$ catalysts for CO methanation in terms of improved metal oxide reducibility, Ni dispersion and resistance to carbon deposition.[67] Nevertheless, the catalytic activity observed in this work is higher than that observed on similar samples containing higher metal loadings. In more detail, the CO_2 conversion reached a maximum of 70 and 75% using 15% Ni/Al_2O_3 promoted with up to 15% Co (ref. 52) (9000 mL g^{-1} h^{-1}) and 15% Ni/Al_2O_3 promoted with up to 20% Ce (30 000 h^{-1}),[63] respectively at 400 °C and $H_2:CO_2$ ratio of 4. This comparison highlights the importance of properly selecting the support and promoter of Ni-based catalysts to achieve beneficial improvement of the catalytic performance in CO_2 methanation.

A comparison of the data obtained in this study (Table 3) can provide valuable insights into the pivotal factors influencing the catalytic performance in CO_2 methanation. Notably, it becomes evident that the most high-performing catalysts, namely $Ni_5/Mg_{63}Al_{37}$ and $Ni_{2.5}Co_{2.5}Ce_3/Mg_{63}Al_{37}$, exhibit a distinctive characteristic of facile reduction, even in the presence of medium basic sites on their surfaces. This affinity for easy reduction emerges as a paramount factor for attaining enhanced catalytic activity. Indeed, the presence of highly dispersed particles with strong basic sites, like in the case of $Ni_{2.5}Co_{2.5}Sr_3/Mg_{63}Al_{37}$ sample, is not sufficient to ensure good catalytic activity because the reduction of this sample required higher temperatures than the highly performing catalysts. Consequently, these findings suggest that incorporating a secondary active phase and/or introducing a promoter holds tangible benefits only when it synergistically facilitates easier reduction.

Conclusions

Given the urgent need for global warming mitigation, CO_2 methanation is a pivotal pathway for the reduction of CO_2 emissions. This study explores the incorporation of MgO to Al_2O_3 as support for Ni and/or Co active phases for the hydrogenation of CO_2 into methane. As the amount of MgO in Al_2O_3 support increases, the NiO reduction shifts towards higher temperatures, resulting in stronger metal–support interaction due to the formation of NiO–MgO solid solution.

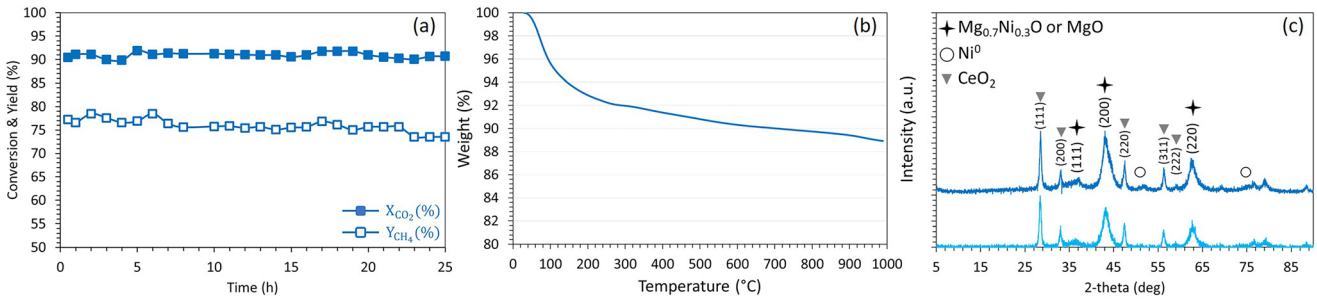

Fig. 14 (a) CO_2 conversion and CH_4 yield, (b) TGA results and (c) XRD profiles (light blue: reduced, dark blue: spent) of $Ni_{2.5}Co_{2.5}Ce_3/Mg_{63}Al_{37}$ catalyst.

Table 3 Summary of data collected on the mono- and bi-metallic catalysts supported on $Mg_{63}Al_{37}$

Sample	TPR peak max. (°C)	TPD basicity	TPD CO_2 desorbed (mmol g^{-1})	Particle size XRD (nm)	CO_2 conv. (%)
$Ni_5/Mg_{63}Al_{37}$	860	Medium	0.29	5.8	92
$Ni_{2.5}Co_{2.5}/Mg_{63}Al_{37}$	925	Medium strong (450 °C)	0.10	5.7	85
$Ni_{2.5}Co_{2.5}Ce_3/Mg_{63}Al_{37}$	863	Medium strong (425 °C)	0.08	6.3	90
$Ni_{2.5}Co_{2.5}Sr_3/Mg_{63}Al_{37}$	880	Medium strong (350 °C)	0.05	5.2	83

The highest catalytic activity of 92% CO_2 conversion and 82% CH_4 yield at 400 °C is achieved using a $Ni_5/Mg_{63}Al_{37}$ sample that shows the highest amount of CO_2 desorbed by CO_2-TPD. The catalytic activity of this sample is higher than those of $Co_5/Mg_{63}Al_{37}$ and $Ni_{2.5}Co_{2.5}/Mg_{63}Al_{37}$, owing to easier reduction on $Ni_5/Mg_{63}Al_{37}$, suggesting that Ni is better than Co under the conditions employed in this work. On the bimetallic sample, the addition of Ce as a promoter is favorable since it boosts the catalytic activity by facilitating the reduction and improving the basicity. This improvement reflects in high catalytic stability for more than 25 hours on steam, with limited carbon deposition and high resistance to sintering. The effect of Sr addition remains limited, probably because the use of an optimized MgO–Al_2O_3 support already enhances the basicity of the catalyst. It is interesting next to evaluate the feasibility of the promising catalysts presented in this study for large-scale applications. This can be achieved by testing them under more industrially attractive conditions, at lower temperatures and higher pressures.

Disclaimer

The views and opinions expressed in this paper do not necessarily reflect those of the European Commission or the Special EU Programmes Body (SEUPB).

Author contributions

Investigation, data acquisition, conceptualization, writing – original draft: Marie-Nour Kaydouh, Nissrine El Hassan, Ahmed I. Osman, Hamid Ahmed, Ahmed S. Al-Fatesh. Methodology, writing, review & editing: Naif Alarifi, Anis H. Fakeeha, Abdulrahman bin Jumah, Ahmed S. Al-Fatesh. Writing – original draft, writing – review & editing; all authors review and edit the manuscript.

Conflicts of interest

There are no conflicts to declare.

Acknowledgements

This research work was funded by Researchers Supporting Project number (RSP2024R368), King Saud University, Riyadh, Saudi Arabia. The authors would like to extend their sincere appreciation to the Researchers Supporting Project number (RSP2024R368), King Saud University, Riyadh, Saudi Arabia. Dr. Ahmed I. Osman wishes to acknowledge the support of The Bryden Centre project (Project ID VA5048), which was awarded by The European Union's INTERREG VA Programme, managed by the Special EU Programmes Body (SEUPB), with match funding provided by the Department for the Economy in Northern Ireland and the Department of Business, Enterprise and Innovation in the Republic of Ireland. This work was also supported by the Lebanese American University President's Intramural Research Fund PIRF I0046.

Notes and references

1 R. Ramezani, L. Di Felice and F. Gallucci, *JPhys Energy*, 2023, **5**, 024010.
2 S. Hafeez, E. Harkou, S. M. Al-Salem, M. A. Goula, N. Dimitratos, N. D. Charisiou, A. Villa, A. Bansode, G. Leeke, G. Manos and A. Constantinou, *React. Chem. Eng.*, 2022, **7**, 795.
3 J. Ren, H. Lou, N. Xu, F. Zeng, G. Pei and Z. Wang, *J. Energy Chem.*, 2023, **80**, 182.
4 T. Burger, P. Donaubauer and O. Hinrichsen, *Appl. Catal., B*, 2021, **282**, 119408.
5 M. Song, L. Shi, X. Xu, X. Du, Y. Chen, W. Zhuang, X. Tao, L. Sun and Y. Xu, *J. CO2 Util.*, 2022, **64**, 102150.
6 L. Karam, M. C. Bacariza, J. M. Lopes, C. Henriques, J. Reboul, N. El Hassan and P. Massiani, *J. CO2 Util.*, 2021, **51**, 101651.
7 S. Danaci, L. Protasova, J. Lefevere, L. Bedel, R. Guilet and P. Marty, *Catal. Today*, 2016, **273**, 234.
8 J. Guilera, J. del Valle, A. Alarcón, J. A. Díaz and T. Andreu, *J. CO2 Util.*, 2019, **30**, 11.
9 H. Chen, Z. Guo, S. Xiang, H. Jianga and Y. Teng, *React. Chem. Eng.*, 2023, **8**, 2632.
10 S. M. Jogdand, P. R. Bedadur, A. Torris, U. K. Kharul, V. Satyam Naidu and R. Nandini Devi, *React. Chem. Eng.*, 2021, **6**, 1655.
11 J. Ashok, S. Pati, P. Hongmanorom, Z. Tianxi, C. Junmei and S. Kawi, *Catal. Today*, 2020, **356**, 471.
12 M. Paviotti, B. Faroldi and L. Cornaglia, *J. Environ. Chem. Eng.*, 2021, **9**, 105173.
13 L. Li, W. Zeng, M. Song, X. Wu, G. Li and C. Hu, *Catalysts*, 2022, **12**, 244.
14 S. V. Moghaddam, M. Rezaei, F. Meshkani and R. Daroughegi, *Int. J. Hydrogen Energy*, 2018, **43**, 19038.
15 L. Karam, C. M. Bacariza, J. M. Lopes, C. Henriques, P. Massiani and N. El Hassan, *Int. J. Hydrogen Energy*, 2020, **45**, 28626.
16 M. Yusuf Shahul Hamid, A. Abdul Jalil, A. Farhana Abdul Rahman and T. Amran Tuan Abdullah, *React. Chem. Eng.*, 2019, **4**, 1126.

17 T. Margossian, K. Larmier, S. M. Kim, F. Krumeich, A. Fedorov, P. Chen, C. R. Müller and C. Copéret, *J. Am. Chem. Soc.*, 2017, **139**, 6919.
18 L. Karam, M. Armandi, S. Casale, V. El Khoury, B. Bonelli, P. Massiani and N. El Hassan, *Energy Convers. Manage.*, 2020, **225**, 113470.
19 K. Jabbour, P. Massiani, A. Davidson, S. Casale and N. El Hassan, *Appl. Catal., B*, 2017, **201**, 527.
20 Y. Guo, J. Lu, Q. Liu, X. Bai, L. Gao, W. Tu and Z.-j. Wang, *Catal. Commun.*, 2018, **116**, 81.
21 J.-N. Park and E. W. McFarland, *J. Catal.*, 2009, **266**, 92.
22 M. Guo and G. Lu, *Catal. Commun.*, 2014, **54**, 55.
23 M. C. Bacariza, I. Graça, S. Bebiano, J. M. Lopes and C. Henriques, *Energy Fuels*, 2017, **31**, 9776.
24 P. Hongmanorom, J. Ashok, G. Zhang, Z. Bian, M. H. Wai, Y. Zeng, S. Xi, A. Borgna and S. Kawi, *Appl. Catal., B*, 2021, **282**, 119564.
25 X. Li, Y. Wang, G. Zhang, W. Sun, Y. Bai, L. Zheng, X. Han and L. Wu, *ChemistrySelect*, 2019, **4**, 838.
26 N. M. Julkapli and S. Bagheri, *Rev. Inorg. Chem.*, 2016, **36**, 1.
27 W. O. Alabi, B. M. Adesanmi, H. Wang and C. Patzig, *Int. J. Hydrogen Energy*, 2024, **51**, 1087.
28 W. O. Alabi, K. O. Sulaiman, H. Wang, Y. Hu and C. Patzig, *J. CO2 Util.*, 2020, **37**, 180.
29 M. Kumar, F. Aberuagba, J. Gupta, K. Rawat, L. Sharma and G. M. Dhar, *J. Mol. Catal. A: Chem.*, 2004, **213**, 217.
30 Y. Lian, H. Wang, Q. Zheng, W. Fang and Y. Yang, *J. Nat. Gas Chem.*, 2009, **18**, 161.
31 A. Vikár, F. Lónyi, A. Makoye, T. Nagy, G. Novodárszki, R. Barthos, B. Szabó, J. Valyon, M. R. Mihályi, D. Deka and H. E. Solt, *Molecules*, 2023, **28**, 3788.
32 G. I. Siakavelas, N. D. Charisiou, A. AlKhoori, S. AlKhoori, V. Sebastian, S. J. Hinder, M. A. Baker, I. V. Yentekakis, K. Polychronopoulou and M. A. Goula, *J. CO2 Util.*, 2021, **51**, 101618.
33 S. Cisneros, L. Santa-Taborda, L. M. Quintana, A. I. M. Rabee, H. Abed, N. Rockstroh, S. Bartling, M. Romero-Sáez, H. Atia, A. B. Dongil, A. Brückner and J. Rabeah, *Chem. Eng. J.*, 2023, **474**, 145646.
34 A. A. M. Abahussain, A. S. Al-Fatesh, N. Patel, S. B. Alreshaidan, N. A. Bamatraf, A. A. Ibrahim, A. Y. Elnour, J. K. Abu-Dahrieh, A. E. Abasaeed, A. H. Fakeeha and R. Kumar, *Nanomater.*, 2023, **13**, 2984.
35 Y. A. Al Baqmaa, A. S. Al Fatesh, A. A. Ibrahim, A. A. Bagabas, F. S. Almubadde, A. I. Alromaeh, J. K. Abu Dahrieh, A. E. Abasaeed and A. H. Fakeeha, *Res. Chem. Intermed.*, 2023, **49**, 5015.
36 A. A. Ibrahim, A. H. Fakeeha, A. E. Abasaeed, I. Wazeer, A. Bentalib, N. S. Kumar, J. K. Abu-Dahrieh and A. S. Al-Fatesh, *Catalysts*, 2023, **13**, 1420.
37 W. Li, Y. Liu, M. Mu, F. Ding, Z. Liu, X. Guo and C. Song, *Appl. Catal., B*, 2019, **254**, 531.
38 W. Li, X. Nie, X. Jiang, A. Zhang, F. Ding, M. Liu, Z. Liu, X. Guo and C. Song, *Appl. Catal., B*, 2018, **220**, 397.
39 T. A. Le, M. S. Kim, S. H. Lee and E. D. Park, *Top. Catal.*, 2017, **60**, 714.
40 Z. Zhang, X. Zhang, L. Zhang, J. Gao, Y. Shao, D. Dong, S. Zhang, Q. Liu, L. Xu and X. Hu, *J. Energy Inst.*, 2020, **93**, 1581.
41 C. Liang, H. Tian, G. Gao, S. Zhang, Q. Liu, D. Dong and X. Hu, *Int. J. Hydrogen Energy*, 2020, **45**, 531.
42 R. Razzaq, H. Zhu, L. Jiang, U. Muhammad, C. Li and S. Zhang, *Ind. Eng. Chem. Res.*, 2013, **52**, 2247.
43 J. J. C. Struijs, V. Muravev, M. A. Verheijen, E. J. M. Hensen and N. Kosinov, *Angew. Chem.*, 2023, **62**, e202214864.
44 M. Gäßler, J. Stahl, M. Schowalter, S. Pokhrel, A. Rosenauer, L. Mädler and R. Güttel, *ChemCatChem*, 2022, **14**, e202200286.
45 J. Tu, H. Wu, Q. Qian, S. Han, M. Chu, S. Jia, R. Feng, J. Zhai, M. Hea and B. Han, *Chem. Sci.*, 2021, **12**, 3937.
46 W. Li, G. Zhang, X. Jiang, Y. Liu, J. Zhu, F. Ding, Z. Liu, X. Guo and C. Song, *ACS Catal.*, 2019, **9**, 2739.
47 B. A. Oni, O. S. Tomomewo, S. E. Sanni and V. O. Ojo, *Mater. Today Commun.*, 2023, **36**, 106802.
48 K. Frikha, L. Limousy, J. Bouaziz, K. Chaari and S. Bennici, *Materials*, 2020, **13**, 4607.
49 M. J. Moradi, G. Moradi, A. Heydarinasab and A. Rashidi, *Mater. Today Commun.*, 2023, **34**, 105226.
50 A. C. Koh, L. Chen, W. K. Leong, B. F. Johnson, T. Khimyak and J. Lin, *Int. J. Hydrogen Energy*, 2007, **32**, 725.
51 Q. Liu, B. Bian, J. Fan and J. Yang, *Int. J. Hydrogen Energy*, 2018, **43**, 4893.
52 P. Shafiee, S. M. Alavi and M. Rezaei, *Int. J. Hydrogen Energy*, 2021, **46**, 3933.
53 N. Fatah, A. Jalil, N. Salleh, M. Hamid, Z. Hassan and M. Nawawi, *Int. J. Hydrogen Energy*, 2020, **45**, 18562.
54 G. Hasrack, M. C. Bacariza, C. Henriques and P. Da Costa, *Catalysts*, 2022, **12**, 36.
55 S. V. Moghaddam, M. Rezaei, F. Meshkani and R. Daroughegi, *Int. J. Hydrogen Energy*, 2018, **43**, 16522.
56 M. Mikhail, P. Da Costa, J. Amouroux, S. Cavadias, M. Tatoulian, M. E. Galvez and S. Ognier, *Appl. Catal., B*, 2021, **294**, 120233.
57 E. H. Cho, Y.-K. Park, K. Y. Park, D. Song, K. Y. Koo, U. Jung, W. R. Yoon and C. H. Ko, *Chem. Eng. J.*, 2022, **428**, 131393.
58 F. Namvar, M. Hajizadeh-Oghaz, M. A. Mahdi, S. H. Ganduh, F. Meshkani and M. Salavati-Niasari, *Int. J. Hydrogen Energy*, 2023, **48**, 3862.
59 C. Liang, X. Hu, T. Wei, P. Jia, Z. Zhang, D. Dong, S. Zhang, Q. Liu and G. Hu, *Int. J. Hydrogen Energy*, 2019, **44**, 8197.
60 M. Guo and G. Lu, *RSC Adv.*, 2014, **4**, 58171.
61 A. Alarcón, J. Guilera, J. A. Díaz and T. Andreu, *Fuel Process. Technol.*, 2019, **193**, 114.
62 J. Y. Do, R. K. Chava, N. Son, J. Kim, N.-K. Park, D. Lee, M. W. Seo, H.-J. Ryu, J. H. Chi and M. Kang, *Catalysts*, 2018, **8**, 413.
63 M.-J. Kim, J.-R. Youn, H. J. Kim, M. W. Seo, D. Lee, K. S. Go, K. B. Lee and S. G. Jeon, *Int. J. Hydrogen Energy*, 2020, **45**, 24595.
64 H. Liu, X. Zou, X. Wang, X. Lu and W. Ding, *J. Nat. Gas Chem.*, 2012, **21**, 703.
65 L. Zhou, Q. Wang, L. Ma, J. Chen, J. Ma and Z. Zi, *Catal. Lett.*, 2015, **145**, 612.

66 M. Varbar, S. M. Alavi, M. Rezaei and E. Akbari, *Res. Chem. Intermed.*, 2022, **48**, 1129.
67 L. Zhang, D.-X. Gu, L. Yi and Y. Zhang, *Catal. Lett.*, 2017, **147**, 1172.
68 P. Summa, K. Ś. Da Costa, Y. Wang, B. Samojeden, M. Rønning, C. Hu, M. Motak and P. Da Costa, *Appl. Mater. Today*, 2021, **25**, 101211.
69 P. Summa, K. Ś. Da Costa, J. Gopakumar, B. Samojeden, M. Motak, M. Rønning, W. Van Beek and P. Da Costa, *Appl. Mater. Today*, 2023, **32**, 101795.
70 R. A. El-Salamony, A. S. Al-Fatesh, K. Acharya, A. A. M. Abahussain, A. Bagabas, N. S. Kumar, A. A. Ibrahim, W. U. Khan and R. Kumar, *Catalysts*, 2023, **13**, 113.
71 S. Ramkumar and G. Rajarajan, *Appl. Phys. A: Mater. Sci. Process.*, 2017, **123**, 401.
72 M. Kaur and K. Pal, *J. Mater. Sci.: Mater. Electron.*, 2020, **31**, 10903.
73 Y. Budipramana, E. Taslim and F. Kurniawan, *ARPN J. Eng. Appl. Sci.*, 2014, **9**, 2074.
74 M. Parvas, M. Haghighi and S. Allahyari, *Arabian J. Chem.*, 2019, **12**, 1298.
75 Q. Pan, J. Peng, T. Sun, S. Wang and S. Wang, *Catal. Commun.*, 2014, **45**, 74.
76 T. Burger, H. M. S. Augenstein, F. Hnyk, M. Döblinger, K. Köhler and O. Hinrichsen, *ChemCatChem*, 2020, **12**, 649.